

Photoacoustic Signal Simulation Using Discrete Particle Approach and Its Application in Tomography

Ravi Prakash, Divakar Badal, Avijit Paul, Deepak Sonker[✉], and Ratan K. Saha[✉], *Member, IEEE*

Abstract—A theoretical framework for photoacoustic (PA) signal simulation using a discrete particle approach is discussed, and the tomographic image reconstruction using such signals is reported. Various numerical phantoms in two dimensions were constructed by inserting monodisperse/polydisperse solid circles/disks of uniform strength occupying regular or random locations within the imaging region. In particular, a blood vessel network phantom was simulated by positioning solid circles mimicking red blood cells randomly within the vessel using a Monte Carlo method. The PA signal from a single disk was obtained by numerically evaluating the analytical formula, and then, such signals from many disks were summed up linearly to generate the resultant signals at detector locations. Classical backprojection and time-reversal algorithms were employed to form reconstructed images. Two model-based approaches, namely impulse response-based (IRB) and interpolation-based (IPB) methods, were also deployed for image reconstruction. Some standard parameters were calculated to assess the performance of these reconstruction algorithms. The simulation results demonstrate that the Monte Carlo method can be applied in practice for the fast simulation of tissue realization keeping microscopic details intact, and accordingly, PA signals can be calculated for photoacoustic tomography (PAT) imaging. Furthermore, the IRB technique produces images with superior quality and outperforms other algorithms.

Index Terms—Monte Carlo method, photoacoustic tomography (PAT), radio frequency line simulation, single particle approach.

I. INTRODUCTION

PHOTOACOUSTIC (PA) imaging is a hybrid imaging modality. It exploits the advantages of optics and acoustics [1]–[3]. The imaging region is irradiated with short laser pulses, and subsequent acoustic signals, generated due to thermoelastic expansion, are utilized for image formation. Currently, it operates in two modes—PA microscopy (PAM) and PA tomography (PAT). PAM can generate the images of objects in the cellular and subcellular regimes with nanometer to micrometer resolution. PAT can produce the images of

tissue structures seating few centimeters deep. PAT technique has found applications in small animal brain imaging [4], [5], vasculature imaging [6], breast imaging [7], [8], sentinel lymph node imaging [9], [10], and molecular imaging [11]–[13].

The purpose of the PAT image reconstruction is to create an image depicting the spatial distribution of initial pressure rise/light absorption function of the illuminated region. Several reconstruction algorithms have been developed so far to achieve this. Analytical approaches include backprojection (BP) algorithm [14] and time-reversal (TR) method [15]. They are, in general, fast and simple techniques. However, they lack to provide quantitative information of the source region. To overcome this problem, model-based approaches have been explored. Although these methods are computationally extensive, they are known to provide accurate quantitative information of the source region. The model matrix (or system matrix) can be built in various ways. For example, it can be accomplished by loading the spatial impulse response of all grid points inside the imaging region at all detector locations [16]–[18]. It is referred to as the impulse response-based (IRB) method in the remaining text. Another group relied on polynomial-based interpolation schemes for the construction of the model matrix [19]–[21]. Essentially, the bilinear interpolation procedure was realized for this purpose. This scheme is termed as the interpolation-based (IPB) method throughout the text.

The well-known k-Wave toolbox has been exclusively used in PA imaging studies [15]. It numerically solves coupled partial differential equations to examine how the PA field evolves with time. It allows to investigate the effects of various factors (e.g., bandwidth, aperture size, organization of the sensors, and width of the input laser pulse) on PA image formation [15], [22], [23]. Almost in all k-Wave implementations, the underlying assumption is that the source region (e.g., blood vessel) is a homogeneous medium containing freely suspending chromophores. Therefore, the cellular aspect of tissue has been ignored. The imaging region in the k-Wave needs to be discretized in the nm scale (≈ 100 nm) if one wants to simulate a tissue by assembling a large number of cells and also considers each cell as a PA source. This is not practical because in that case, computation time and memory requirement would become unrealistically high. On the contrary, a theoretical model has been developed by exploiting

Manuscript received July 1, 2020; accepted September 5, 2020. Date of publication September 9, 2020; date of current version February 24, 2021. (Corresponding author: Ratan K. Saha.)

The authors are with the Department of Applied Sciences, Indian Institute of Information Technology Allahabad, Allahabad 211015, India (e-mail: ratank.saha. @.iiita.ac.in).

Digital Object Identifier 10.1109/TUFFC.2020.3022937

the cellular aspect of blood [24]. The PA field from a single red blood cell (RBC) [approximated as a fluid sphere (in three dimensions)] suspended in another fluid medium can be calculated by employing a frequency-domain approach [25]. The PA field from blood has been obtained by summing the fields emitted by the individual RBCs. This is called the discrete/single particle approach. This model assumes that the light absorption takes place in the molecular level, but acoustic emission takes place in the cellular level. Furthermore, in this picture, hemoglobin molecules are bounded within RBCs, and their concentration (inside a cell) and oxygen saturation states define the amplitude of the PA field emitted by a cell. We previously applied this approach for tissue simulation (mostly blood tissue simulation comprised of randomly distributed RBCs) and signal calculation in order to study how blood pathologies affect PA spectral features [26]–[30].

The objective of this article is to apply discrete particle approach for PA signal simulation and then to perform PAT image reconstruction using such signals. Essentially, several numerical phantoms in two dimensions were constructed by placing single/multiple, monodisperse/polydisperse solid circles (also referred to as disk in the text) with uniform strength occupying regular/random locations within the imaging region. In particular, a blood vessel network was created by randomly inserting solid circles of radius $2.75\text{-}\mu\text{m}$ mimicking RBCs inside the vessel. A Monte Carlo technique known as the random sequential adsorption technique was implemented to generate the random locations of the solid circles [31], [32]. It offers a quick method for simulating tissue configurations preserving structural details in the cellular level. The PA signal from a solid circle for a delta function laser pulse was calculated by numerically evaluating the exact formula. The resultant signals at the detector locations were computed by linearly adding the tiny signals emitted by the individual disks. The BP, TR, IRB, and IPB algorithms were implemented for image reconstruction. Some standard parameters were computed to quantitatively assess the performance of each method. The discrete particle approach can be adapted in practice for PA signal simulation, and the IRB technique has been found to produce the best reconstructed images.

The organization of the rest of this article is as follows. Section II elaborates the theoretical framework utilized for forward signal simulation. The theoretical aspects of the BP, TR, IRB, and IPB reconstruction methods are briefly described in this section as well. The quantitative methods to compare the performance of the reconstruction techniques are also highlighted in this section. The numerical simulations are detailed in Section III. Section IV portrays the numerical results. Finally, the discussion and conclusions of this work are presented in Section V.

II. FORWARD AND INVERSE PROBLEM FRAMEWORKS

A. PA Signal Calculation

The time-dependent PA wave equation under the restriction of thermal and stress confinements is given by [25]

$$\nabla^2 p(\mathbf{r}, t) - \frac{1}{v_s^2} \frac{\partial^2 p(\mathbf{r}, t)}{\partial t^2} = -\frac{\beta}{C_p} \frac{\partial H(\mathbf{r}, t)}{\partial t} \quad (1)$$

where β , C_p , v_s , and H are the isobaric thermal expansion coefficient, specific heat, speed of sound within the source region, and heat delivered by the incident laser beam to the sample per unit time and volume, respectively. The solution to (1) in the frequency domain for a homogeneous infinite circular cylinder surrounded by a fluid medium after satisfying the continuity of pressure and normal component of particle velocity at the boundary becomes [25]

$$\tilde{p}_f(\hat{q}) = \frac{i\mu\beta I_0 v_s a}{C_p} \left[\frac{J_1(\hat{q}) H_0^{(1)}(\hat{c}\hat{r}\hat{q})}{\hat{q} [J_1(\hat{q}) H_0^{(1)}(\hat{c}\hat{q}) - \hat{\rho}\hat{c} J_0(\hat{q}) H_1^{(1)}(\hat{c}\hat{q})]} \right] \quad (2)$$

where μ and a are the light absorption coefficient and radius of the source, respectively; I_0 and ω denote intensity and modulation frequency of the exciting laser beam, respectively; J_0 and J_1 indicate the Bessel function of zeroth and first orders, respectively; and similarly, $H_0^{(1)}$ and $H_1^{(1)}$ refer to the Hankel function of first kind of the same orders, respectively. The notations ρ_s , ρ_f , and v_f state the density of the source, density, and speed of sound of the surrounding medium, respectively. The dimensionless quantities can be defined as, $\hat{q} = (\omega a / v_s)$, $\hat{\rho} = (\rho_s / \rho_f)$, $\hat{c} = (v_s / v_f)$, $\hat{r} = (r_0 / a)$. Here, r_0 is the distance of the detector (i.e., field point) from the center of the source. The subscripts s and f represent the source and fluid medium, respectively. Note that (2) is a function of r_0 only (independent of the z coordinate of the field point). Therefore, 3-D problem essentially reduces to a 2-D problem, and consequently, (2) can be used to estimate the PA field produced by a solid circle. The time-dependent pressure by a solid circle in the surrounding fluid medium for a delta function input laser pulse in the far-field region ($r_0 \gg a$) can be expressed as [25]

$$p_f^{(1)}(\mathbf{r}_0, t) \approx \frac{i\mu\beta v_s a F}{2\pi C_p} \times \sqrt{\frac{2v_f}{\pi r_0}} \times \int_{-\infty}^{\infty} d\omega \times \frac{\omega^{-\frac{1}{2}} J_1(\hat{q}) e^{i(k_f r_0 - \frac{\pi}{4})} e^{-i\omega t}}{\hat{q} [J_1(\hat{q}) H_0^{(1)}(\hat{c}\hat{q}) - \hat{\rho}\hat{c} J_0(\hat{q}) H_1^{(1)}(\hat{c}\hat{q})]}, \quad (3)$$

with F as the fluence of the heating pulse, k_f is the wavenumber, and the superscript (1) of p_f states that signal is generated by a single particle.

The PA signal in the asymptotic region for a many particle system can be expressed as a linear superposition of signals emitted by the individual disks as

$$p_f^{(N)}(\mathbf{r}_0, t) \approx \frac{i\mu\beta v_s F}{2\pi C_p} \times \sqrt{\frac{2v_f}{\pi r_0}} \times \int_{-\infty}^{\infty} d\omega \sum_{n=1}^N a_n \omega^{-\frac{1}{2}} J_1(\hat{q}_n) \times \frac{1}{\hat{q}_n} \times \frac{e^{i(k_f r_0 - \frac{\pi}{4} - \omega t)} e^{-i\mathbf{k}_f \cdot \mathbf{r}_n}}{[J_1(\hat{q}_n) H_0^{(1)}(\hat{c}\hat{q}_n) - \hat{\rho}\hat{c} J_0(\hat{q}_n) H_1^{(1)}(\hat{c}\hat{q}_n)]} \quad (4)$$

where \mathbf{r}_n and a_n are the position vector and radius of the n th disk, and \mathbf{k}_f defines the direction of measurement with

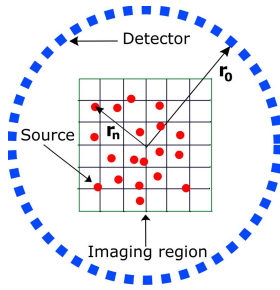


Fig. 1. Representative diagram of the simulation geometry.

$\hat{q}_n = (\omega a_n / v_s)$. The superscript (N) indicates that the illuminated region contains N number of disks. A representative diagram is shown in Fig. 1. This is called the discrete particle approach, where the resultant PA signal is simulated by adding the tiny signals produced by the individual particles. Equations (3) and (4) provide signals with infinite bandwidth. The corresponding bandlimited (measured) signal can be generated using a cosine Gabor filter as [27]

$$p(\mathbf{r}_0, t) = \begin{cases} \text{Re}(p_f^{(1)}(\mathbf{r}_0, t)) * \frac{\sigma e^{-\frac{\sigma^2 t^2}{2}}}{\sqrt{2\pi}} \cos(2\pi f_0 t) \\ \text{Re}(p_f^{(N)}(\mathbf{r}_0, t)) * \frac{\sigma e^{-\frac{\sigma^2 t^2}{2}}}{\sqrt{2\pi}} \cos(2\pi f_0 t) \end{cases} \quad (5)$$

where $*$ denotes the convolution operation, Re indicates real part of the signal, f_0 is the center frequency, and σ is related to the -6 -dB bandwidth of the transducer. In this work, (5) has been computed to yield bandlimited PA signal generated by a single disk or an ensemble of disks at a detector location.

B. Image Reconstruction

The heating function can be expressed as $H(\mathbf{r}, t) = A(\mathbf{r})\delta(t)$ with $A(\mathbf{r})$ as the spatial light absorption function, and $\delta(t)$ is the Dirac delta function. Therefore, (1) becomes [1]

$$\nabla^2 p(\mathbf{r}, t) - \frac{1}{v_s^2} \frac{\partial^2 p(\mathbf{r}, t)}{\partial t^2} = -\frac{p_0(\mathbf{r})}{v_s^2} \frac{d\delta(t)}{dt} \quad (6)$$

where $p_0(\mathbf{r}) = \Gamma A(\mathbf{r}) = \Gamma \mu(\mathbf{r}) F$ is the initial pressure rise due to light absorption with $\Gamma = v_s^2 \beta / C_P$ as the Grüneisen parameter, which is taken as constant throughout the imaging region. The purpose of the PAT imaging is to produce a spatial map of $p_0(\mathbf{r})$ or $A(\mathbf{r})$ using pressure data $p(\mathbf{r}_0, t)$ measured at \mathbf{r}_0 .

1) *Analytical Approach*: The rigorous reconstruction formulas for planar, cylindrical, and spherical recording surfaces are deduced in [33]. However, these expressions contain Fourier integrations or series summations and are generally inconvenient for implementation. A relatively simple time-domain reconstruction formula known as the universal BP formula has been derived by the same group for the above-mentioned detector geometries [14]. The PA pressure predicted by the BP algorithm is given by [14]

$$p_0^b(\mathbf{r}) = \int_{\Omega_0} b\left(\mathbf{r}_0, t = \frac{|\mathbf{r} - \mathbf{r}_0|}{v_f}\right) d\Omega_0 / \Omega_0 \quad (7)$$

where

$$b(\mathbf{r}_0, t) = 2p(\mathbf{r}_0, t) - 2t \frac{\partial p(\mathbf{r}_0, t)}{\partial t} \quad (8)$$

is the BP term, and $d\Omega_0$ is the solid angle subtended by the detector element at the reconstruction point \mathbf{r} ; Ω_0 is the total solid angle subtended by the whole detector setup.

Another popular approach is the TR method. In this case, the PA wave equation is solved with the appropriate initial and boundary conditions to estimate actual pressure distribution at $t = 0$. The numerical values of pressure are taken as zeros at all field points, and the measured data provide boundary values. This method works well if the density and speed of sound of the imaging region remain spatially invariant.

2) *Model-Based Approach*: In this approach, PAT image reconstruction is expressed as a system of linear equations as [16]

$$\Lambda z = p, \quad \Lambda \in \mathbb{R}^{m \times l}, \quad z \in \mathbb{R}^l, \quad p \in \mathbb{R}^m \quad (9)$$

where Λ is the model matrix (or system matrix), z is the unknown representing spatial map of initial pressure rise/light absorption function, and p is a long column vector constructed by stacking measured pressure data.

In general, the model matrix depends on the speed of sound of the medium, geometry of the PAT system, and properties of the individual detectors (e.g., frequency response and sensitivity profile of the receiving aperture). It is a large matrix, and in general, it is not a square matrix rendering it to be noninvertible. Because of this, it is not possible to obtain a direct solution of z . One of the methods is to demand the least square error as [16]

$$z_{\text{sol}} = \text{argmin} \|\Lambda z - p\|_2^2 \quad (10)$$

where $\|\cdot\|_2$ denotes l_2 norm. Another approach is to employ the Moore–Penrose pseudo inverse

$$z_{\text{sol}} = \Lambda^\dagger p \quad (11)$$

where $\Lambda^\dagger = (\Lambda^T \Lambda)^{-1} \Lambda^T$ with T is the transpose operation of a matrix. Note that the left inverse exists if $m > l$. These two methods work faithfully for full view data set (i.e., when data acquisition takes place over 360° around the imaging region in two dimensions) facilitating a large number of projections. For limited view data set, it is better to use the Tikhonov regularization scheme to yield an accurate estimate, and it is accomplished by minimizing the following cost function [16]:

$$\Sigma = \|\Lambda z - p\|_2^2 + \lambda^2 \|Lz\|_2^2 \quad (12)$$

where λ is referred to as the regularization parameter, and L is a derivative operator. Smoothness of the solution depends on these two parameters. The L matrix can be built using a spatial normalized Laplacian filter with a kernel (K_L) [20]

$$K_L = \frac{1}{9} \begin{pmatrix} -1 & -1 & -1 \\ -1 & 8 & -1 \\ -1 & -1 & -1 \end{pmatrix}. \quad (13)$$

In this work, z_{sol} has been obtained by minimizing Σ as given in (12), whereas two different methods have been implemented for generating the Λ matrix.

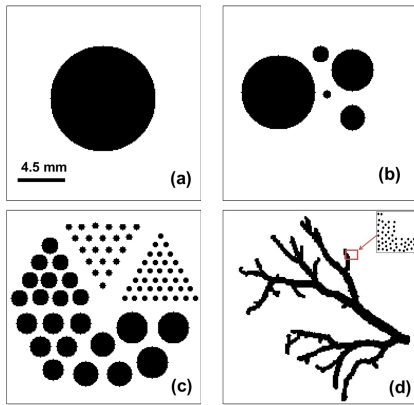


Fig. 2. Demonstration of the numerical phantoms. (a) Disk phantom. (b) Multiple disks phantom. (c) Derenzo phantom. (d) Vasculature phantom.

III. NUMERICAL SIMULATION

A. Phantom Construction

Four numerical binary phantoms were constructed to compare the performance of the reconstruction techniques. These phantoms are single disk, polydisperse multiple disks, Derenzo phantom, and a blood vessel network as shown in Fig. 2(a)–(d), respectively. A uniform disk with a radius of 5 mm was located at the center of the imaging region in the first phantom. Five different disks with radii 0.4, 0.8, 1.2, 2.0, and 3.5 mm were positioned arbitrarily within the illuminated region in the second phantom. The coordinates of the centers of the disks were stored. Six different sets of disks (with radii 0.25, 0.30, 0.8, 1.0, 1.2, and 1.5 mm) were placed in the third phantom occupying a triangular region by each group as shown in Fig. 2(c). In this case, also, position coordinates of each disk were recorded.

The fourth phantom was constructed in the following manner. A binary image of a blood vessel network of $18 \times 18 \text{ mm}^2$ size was scanned at 600 dots per inch ($\approx 42.3 \text{ }\mu\text{m}$ as the grid spacing). Therefore, the image matrix contained 425×425 pixels. A value of 1 was tagged to the grid points inside the network; otherwise, 0 was assigned. The number of grid points inside the phantom was computed to obtain the area occupied by the blood vessel network. It occupied $\approx 35.3 \text{ mm}^2$ out of 324 mm^2 . A total number of 594 275 disks with radius $2.75\text{-}\mu\text{m}$, mimicking RBCs, were thrown randomly into the region inside the vessel. Hence, the hematocrit level was calculated to be 0.4. A Monte Carlo algorithm known as the sequential adsorption technique was applied to generate the random locations of RBCs [31], [32]. In this approach, a random position for a RBC was proposed and was accepted if it did not overlap with cells that were already positioned. If it did not satisfy the nonoverlapping condition, a new position was proposed.

To develop an efficient computer program, the imaging region was divided into 425 rectangular strips (along the x -axis) each of size $42.3 \times 18\,000 \text{ }\mu\text{m}^2$. We began positioning of cells from the extreme left and moved to the right gradually. Now consider a strip. Cells were placed sequentially within the branch/branches of the phantom inside that strip.

Nonoverlapping condition with cells (already positioned) inside that strip as well as those inside the previous (neighboring) strip was tested before placing a cell. Therefore, the possibility of overlapping of cells at the boundary was removed. This approach reduced execution time significantly because nonoverlapping condition was checked for a small number of cells (only those inside these two strips). After that, cells were placed in the next strip. This scheme was implemented previously by us for the simulation of blood tissue realizations in three dimensions [27]. It may be noted that RBCs could also be randomly thrown inside the entire vessel. However, in that case, nonoverlapping condition with all existing cells (occupying valid locations) would need to be examined. It is a computationally extensive task. Furthermore, execution time would grow nonlinearly since the number of cells to be considered would grow with iteration. Plots of the coordinates of RBCs generated using the Monte Carlo technique are shown in Fig. 2(d), which mimicked the structure of the source well. Furthermore, the spatial organization of cells of a small portion within the red box is shown in the inset to demonstrate the microscopic nature of the vessel. A MATLAB code was written for this purpose, and it took $\approx 105 \text{ s}$ in a virtual machine to generate the random locations of RBCs (RAM: 256 GB, cores: 80, clock speed: 2.19 GHz, processor: Intel Core (Skylake, IBRS), OS: CentOS).

B. Signal Calculation

The density and speed of sound of the surrounding medium were chosen as $\rho_f = 1000 \text{ kg/m}^3$ and $v_f = 1500 \text{ m/s}$, respectively. The numerical values of these parameters for the source region were considered to be the same. In addition, the thermomechanical parameters for the source region were taken as $I_0 = 1$, $\beta = 1$, $C_P = 1$, and $\mu = 1$ as these parameters only control the amplitude of the PA signal and do not influence spectral properties [24]. The PA signal was calculated at a distance of 5 cm from the center of the imaging region (see Fig. 3) from $t = 0$ to $50 \text{ }\mu\text{s}$ using a sampling frequency of 2000 MHz ($\Delta t = 0.5 \text{ ns}$). The contributing frequencies were varied from 1 kHz to 1000 MHz with an increment of 10 kHz. The numerical integration in (3) or (4) was carried out using the trapezoidal rule. The initial data length at a detector location was 100 000. Such a signal was filtered employing (5) when $f_0 = 2.25 \text{ MHz}$ and 70% as the -6-dB bandwidth and, subsequently, down sampled 40 times (using the decimate function of MATLAB), providing a final data length of 2500 and $\Delta t = 20 \text{ ns}$. A 40-dB noise level was added with the numerically generated signal. This procedure was followed to compute the PA signals at 100 detector locations uniformly distributed within an angular range of $0\text{--}2\pi$ for each phantom. The discrete particle approach took approximately 250 s to generate the PA signals for 100 detector locations. The simulated signals were used for image reconstruction.

C. Image Generation

Image reconstruction was performed for a region of $18 \times 18 \text{ mm}^2$ with respect to the scanning center, and this region

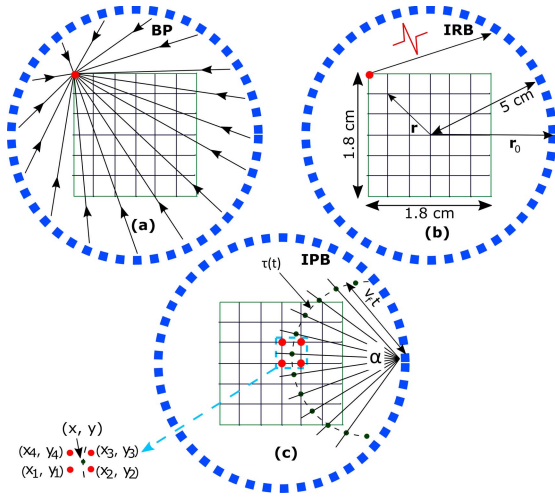


Fig. 3. Graphical illustration of the reconstruction algorithms. (a) BP. (b) IRB. (c) IPB.

was divided into 181×181 grid points. The grid spacing became $dx = dy = 100 \mu\text{m}$. After that, the BP term as given in (8) was computed for each detector, and subsequently, (7) was evaluated for all detectors for each grid point. A schematic is shown in Fig. 3(a). It might be mentioned here that we did not include any angle-dependent factor for each detector at each grid point while calculating $d\Omega_0$ since we considered point detectors, and also, we took $\Omega_0 = 2\pi$ as image reconstruction was performed in two dimensions. The reconstructed images for the TR technique were formed deploying the pertinent function of the k-Wave toolbox [15].

For the IRB algorithm, Λ matrix was constructed by adapting the method described in [16]. The PA signal from a disk with $50\text{-}\mu\text{m}$ radius, placed at a corner grid point as shown in Fig. 3(b), was calculated at the location of the first detector. This signal was treated as the reference signal and could also be thought of as the spatial impulse response for the first detector for the top leftmost corner pixel. This signal was loaded into the Λ matrix (first column, rows from 1 to 2500). The signals from all other grid points (by traversing column wise starting from the top row, second leftmost corner) to the first detector were generated by properly scaling and shifting of the reference PA signal. Accordingly, all the columns from 2 to 32761 and rows from 1 to 2500 of the Λ matrix were filled up. Similarly, the PA signals were calculated for all grid points traveling in the identical manner for the second detector and copied in the Λ matrix (rows from 2501 to 5000 and columns from 1 to 32761). This procedure was followed for the remaining 98 detectors. The size of the Λ matrix was 25000×32761 (≈ 61 GB). The PA signals simulated at 100 detector locations for a numerical phantom as described above were stacked columnwise to form the p matrix, whose size was 25000×1 .

As the size of the Λ matrix became very large, we did not consider 2500 data points in each signal rather we took 941 data points (array locations from 1200 to 2140) providing $m \times l = 94100 \times 32761$. The same length was also considered while filling the p matrix. This approach significantly reduced

the size of the Λ matrix (≈ 23 GB) *viz-a-viz* computation time. This step did not affect the results because we discarded many zeros (or noise) from both sides. The size of the L matrix could be computed to be $l^2 \times l^2 = 32761 \times 32761$ (≈ 8 GB). The singular value decomposition of the Λ matrix was accomplished, and accordingly, optimal regularization parameter (λ) was obtained. This parameter was utilized to perform the Tikhonov regularization for yielding a good estimate of z_{sol} . The last three steps were realized using `cgsvd`, `l_curve`, and Tikhonov functions of MATLAB-based regularization toolbox [34]. The singular value decomposition took around 1 h 30 min to complete, and after that, image reconstruction was finished within nearly 40 s in the same machine for each phantom.

The details of the IPB reconstruction technique can be found in [20]. Essentially, the solution of (6) in two dimensions can be given by the Poisson-type integral as [20]

$$\begin{aligned} p(\mathbf{r}_0, t) &= \frac{1}{4\pi v_f} \frac{\partial}{\partial t} \int_{\tau(t)} \frac{p_0(\mathbf{r})}{|\mathbf{r}_0 - \mathbf{r}|} d\tau(t) \\ &= \frac{\Gamma}{4\pi v_f} \frac{\partial}{\partial t} \int_{\tau(t)} \frac{A(\mathbf{r})}{|\mathbf{r}_0 - \mathbf{r}|} d\tau(t) \end{aligned} \quad (14)$$

where $\tau(t)$ is the arc length within the illuminated region, for which $|\mathbf{r}_0 - \mathbf{r}| = v_f t$. Equation (14) states that signals from the points lying on this arc add up coherently at \mathbf{r}_0 as shown in Fig. 3(c), and the time derivative of the resultant signal gives rise to the PA pressure at that point. Equation (14) can be further decomposed as [20]

$$p(\mathbf{r}_0, t) \approx \frac{I_{\text{abs}}(t + \Delta t) - I_{\text{abs}}(t - \Delta t)}{2\Delta t} \quad (15)$$

with

$$I_{\text{abs}}(t) = \int_{\tau(t)} \frac{p_0(\mathbf{r})}{|\mathbf{r}_0 - \mathbf{r}|} d\tau(t). \quad (16)$$

It is evident from (15) that points on the two arcs indeed participate in producing the PA pressure at \mathbf{r}_0 at time t . For the former arc, $|\mathbf{r}_0 - \mathbf{r}| = v_f(t + \Delta t)$, and it is $v_f(t - \Delta t)$ for the later arc.

The forward modeling approach can be used to solve the inverse problem. It means that the PA pressure on the points lying on these two arcs can be found from the measured pressure at \mathbf{r}_0 at time t . Furthermore, the PA pressure on the neighboring grid crossings for each point on the arc can be estimated using interpolation technique. In this work, bilinear interpolation has been implemented for this purpose. The schematic is shown in Fig. 3(c). Essentially, the minimum angular region (i.e., α) that was required to entirely enclose the imaging region (considering all detectors) was calculated. This angular region was divided into 200 subangles. Therefore, 201 equidistant points (including the starting point) on the arc were considered. The PA pressure at a point (x, y) is related to the pressure at the four points (denoted by z_1, z_2, z_3 and z_4) as [20]

$$\begin{aligned} z(x, y) &= (1 - \Delta x_1)(1 - \Delta y_1)z_1 + \Delta x_1(1 - \Delta y_1)z_2 \\ &\quad + \Delta x_1\Delta y_1z_3 + (1 - \Delta x_1)\Delta y_1z_4 \end{aligned} \quad (17)$$

where $\Delta x_1 = (x - x_1)/dx$, and $\Delta y_1 = (y - y_1)/dy$. In this way, pressure at all the grid crossings bounding the points on

the arc can be determined. This procedure can be repeated for all arcs, which, in general, can be written in a matrix form as [20]

$$p(\mathbf{r}_0, t_j) = \sum_l W_{jl} z_l \quad (18)$$

where pressure is calculated at t_j th instant, W_{jl} is the corresponding coefficient, and l indicates the grid number (it is made by traversing columnwise starting from the top row, leftmost corner as described above). In this work, the model matrix Λ was built by choosing appropriate W_{jl} for each grid crossing. It might be mentioned here that the coefficients became positive for the grid crossings, enclosing points on the arc for which $|\mathbf{r}_0 - \mathbf{r}| = v_f(t_j + \Delta t)$. However, coefficients for the grid crossings corresponding to the other arc for which $|\mathbf{r}_0 - \mathbf{r}| = v_f(t_j - \Delta t)$ were negative. The coefficients were considered to be zero for grid crossings which did not bound the arcs. This procedure was followed for all detectors.

D. Analysis of Performance of the Reconstruction Methods

The next step was to compute various parameters for the quantitative estimation of the performance of the reconstruction methods. These are the standard parameters and have also been used in the other works. The parameters are briefly summarized here.

1) *Error Norm (ERN)*: The ERN is defined as [18]

$$\text{ERN} = \|z - z_{\text{sol}}\|_2 \quad (19)$$

where z and z_{sol} are the nominal and estimated values, respectively. ERN becomes zero for perfect reconstruction.

2) *Pearson Correlation Coefficient (PCC)*: The PCC can quantify the similarity between two images and is given by [18]

$$\text{PCC} = \frac{\text{COV}(z, z_{\text{sol}})}{\sigma_z \sigma_{z_{\text{sol}}}} \quad (20)$$

where COV denotes the covariance between two matrices, σ_z is the standard deviation of the original image, and $\sigma_{z_{\text{sol}}}$ is that of the reconstructed image. Its numerical value varies from -1 to 1 . Higher the value of PCC, better is the reconstruction.

3) *Contrast to Noise Ratio (CNR)*: The CNR is a parameter that can be used to quantify how good a reconstructed image is compared to the original image. It is expressed as [18]

$$\text{CNR} = \frac{\eta_{\text{roi}} - \eta_{\text{back}}}{(\sigma_{\text{roi}}^2 n_{\text{roi}} + \sigma_{\text{back}}^2 n_{\text{back}})^{\frac{1}{2}}} \quad (21)$$

where η is the mean and σ is the standard deviation; the subscripts “roi” and “back” refer to the region of interest and background in the reconstructed image; $n_{\text{roi}} = A_{\text{roi}}/A_{\text{total}}$ and $n_{\text{back}} = A_{\text{back}}/A_{\text{total}}$ with A_{total} as the total number of pixels in the original/reconstructed image, A_{roi} is the total number of pixels in the original image with $p_0 \neq 0$, and A_{back} is the total number of pixels in the original image with $p_0 = 0$. The “roi” becomes easily distinguishable with respect to the “back” if CNR is large. In this work, 48 pixels were chosen in the “roi” to calculate its η and σ , whereas 169 pixels were considered in the “back” to determine the same parameters.

4) *Signal to Noise Ratio (SNR)*: The SNR can be computed as

$$\text{SNR} = 20 \log_{10} \left(\frac{M}{\sigma_{\text{back}}} \right) \quad (22)$$

where M is the peak pressure of the “roi.”

E. Simulation Using k-Wave Toolbox

To validate the results presented in this work, we also performed simulations using the k-Wave toolbox [15]. The computational grid size was taken as 1101×1101 with $dx = dy = 100 \mu\text{m}$. The width of the perfectly matched layer was ten grid points. The PA signals were calculated at a distance of 5 cm from the imaging/scanning center at 100 detector locations. The length of the time series data for each detector was 2500 with $\Delta t = 20$ ns. Accordingly, the Courant–Friedrichs–Lewy number ($c\Delta t/dx$) became 0.3. The same numerical phantoms were loaded sequentially in the k-Wave toolbox, and the forward data were generated. Each forward simulation took approximately 13 min to run. After that, the reconstruction formulas mentioned above were used exactly following the same steps for image formation.

IV. NUMERICAL RESULTS

The reconstructed images generated by the BP, TR, IRB, and IPB algorithms are shown in Fig. 4 when forward data have been generated by the single particle approach. The corresponding image profiles along the cyan lines as drawn in the BP images are shown in the last column of this figure as well. Each image is normalized by its maximum pressure value. It can be seen from Fig. 4 that the source regions are reproduced well by the reconstruction methods considered in this study. It is clear from Fig. 4(a)–(e) that a solid circle is converted to a blurred circle due to reconstruction. It occurs because bandlimited signals have been employed for image reconstruction. Fig. 4(b) exhibits that prominent streak artifact build up in the TR reconstruction, but it is relatively small in the other images [Fig. 4(a), (c), and (d)]. This artifact may become negligible with an increasing number of projections. The pressure at the boundary is faithfully estimated in all reconstructed images [see Fig. 4(e)]. However, the same quantity inside the disk is best determined by the IRB algorithm [see the purple line in Fig. 4(e)]. The prediction made by the TR method is also close to that of IRB scheme at least at the central region as apparent from Fig. 4(e) (green line). The PA pressure inside the source for the BP and IPB techniques is predicted to be very small, and it is far away from the nominal value (red and blue lines with respect to the black line).

Fig. 4(f)–(i) and (k)–(n) shows the reconstructed images of a series of solid disks with different radii. As observed in the previous case, IRB provides the best spatial map of initial pressure distribution for all disks. The images generated by the other three methods look almost comparable. Furthermore, in these algorithms, initial pressure rise inside small objects (with radius 0.4 mm in the second row and radius 0.3 mm in the third row) is reproduced with the highest accuracy, whereas deviations with respect to the ground truths

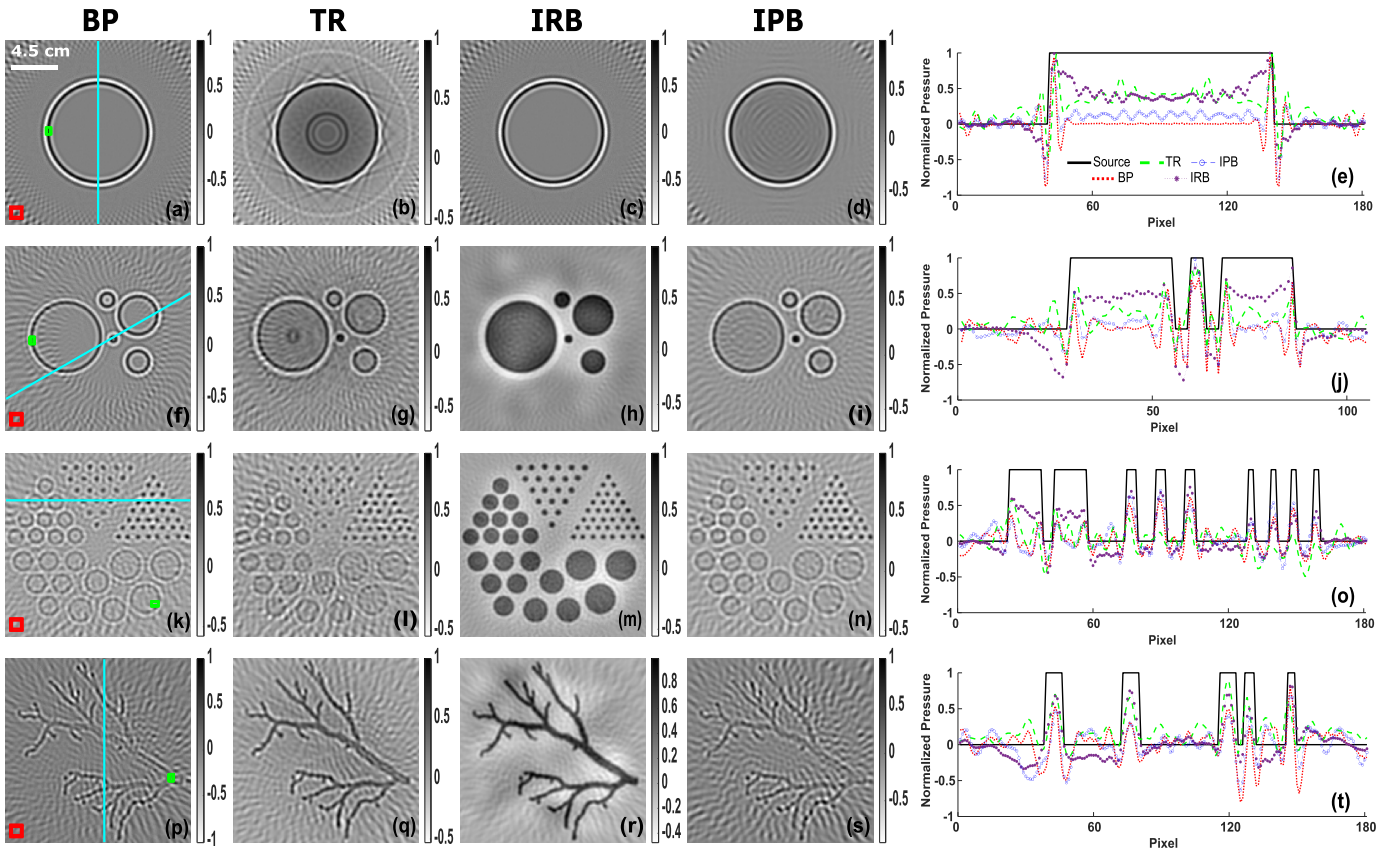


Fig. 4. Reconstructed images of the numerical phantoms considered in this study using the PA signals generated by the single particle approach. Simulated images formed by the BP, TR, IRB, and IPB algorithms of the single disk phantom shown in (a)–(d), respectively. (e) Line plots [pixel values along the cyan line as shown in (a)] for these images. (f)–(j) Same as (a)–(e) but for the multiple disks phantom. (k)–(o) Same as (a)–(e) but for the Derenzo phantom. (p)–(t) Same as (a)–(e) but for the vasculature phantom. Quantitative analysis has been performed based on the indicated roi (pixels inside the green box) and background (pixels inside the red box) regions.

are noticeable for large disks. This can be clearly noticed in Fig. 4(j) and (o). Moreover, the shapes of the smallest objects with a radius of 0.25 mm are retained well in the reconstructed images [Fig. 4(k)–(n)], but the estimated PA pressure distribution within this group of disks is less than the nominal value and also prediction is inferior compared to that of the other set with radius 0.3 mm [see Fig. 4(o)]. All the reconstruction algorithms facilitate similar pressure maps inside the source for the vasculature phantom as evident from Fig. 4(p)–(s) and more precisely from Fig. 4(t). However, background noise has been greatly suppressed in the IRB reconstruction.

The performance of the reconstruction techniques has been assessed quantitatively in this work and shown in Table I. The numerical values of the local parameters (CNR and SNR) for the source have been computed from the region enclosed by the green box, and the pixels within the red box are considered as background region (see the first column of Fig. 4). The numerical values of various parameters (rows 2–5, column 3) confirm that the BP algorithm is the least effective among all for the disk and multiple disk phantoms. The TR algorithm has a slight edge over the IPB technique if we consider the first phantom (compare columns 4 and 6 and rows from 2 to 5). However, they become comparable for the second phantom (compare columns 4 and 6 and rows from 6 to 9). Computed numerical values fluctuate for the third phantom in these three

TABLE I
QUANTITATIVE COMPARISON OF PERFORMANCE OF DIFFERENT RECONSTRUCTION METHODS FOR PA SIGNALS GENERATED BY THE SINGLE PARTICLE APPROACH

Phantom	Metric	BP	TR	IRB	IPB
Disc	ERN	90.86	61.71	52.41	78.83
	PCC	0.16	0.67	0.88	0.44
	CNR	0.37	0.95	2.58	0.86
	SNR (dB)	11.46	20.46	32.96	11.12
Multiple discs	ERN	76.90	64.82	51.23	69.53
	PCC	0.21	0.43	0.80	0.42
	CNR	0.54	2.24	2.43	1.15
	SNR (dB)	17.14	18.08	30.86	14.58
Derenzo	ERN	87.12	83.83	61.11	83.85
	PCC	0.40	0.37	0.88	0.50
	CNR	0.48	0.62	7.33	0.89
	SNR (dB)	16.59	9.93	26.05	13.68
Vasculature	ERN	66.87	51.94	41.49	67.42
	PCC	0.30	0.57	0.81	0.31
	CNR	0.03	3.42	10.95	0.24
	SNR (dB)	12.83	17.59	30.39	7.77

reconstruction methods (as given in columns 3, 4, and 6 and rows from 10 to 13), and hence, a comparison is not trivial. In the case of vasculature phantom, TR performs better than the BP and IPB techniques. For instance, PCC for TR is equal to 0.57 and is greater than that of BP (0.30) and IPB (0.31). The estimated parameters (column 5) confirm that the IRB protocol provides much superior reconstruction than those of the other methods. This is in accordance with Fig. 4.

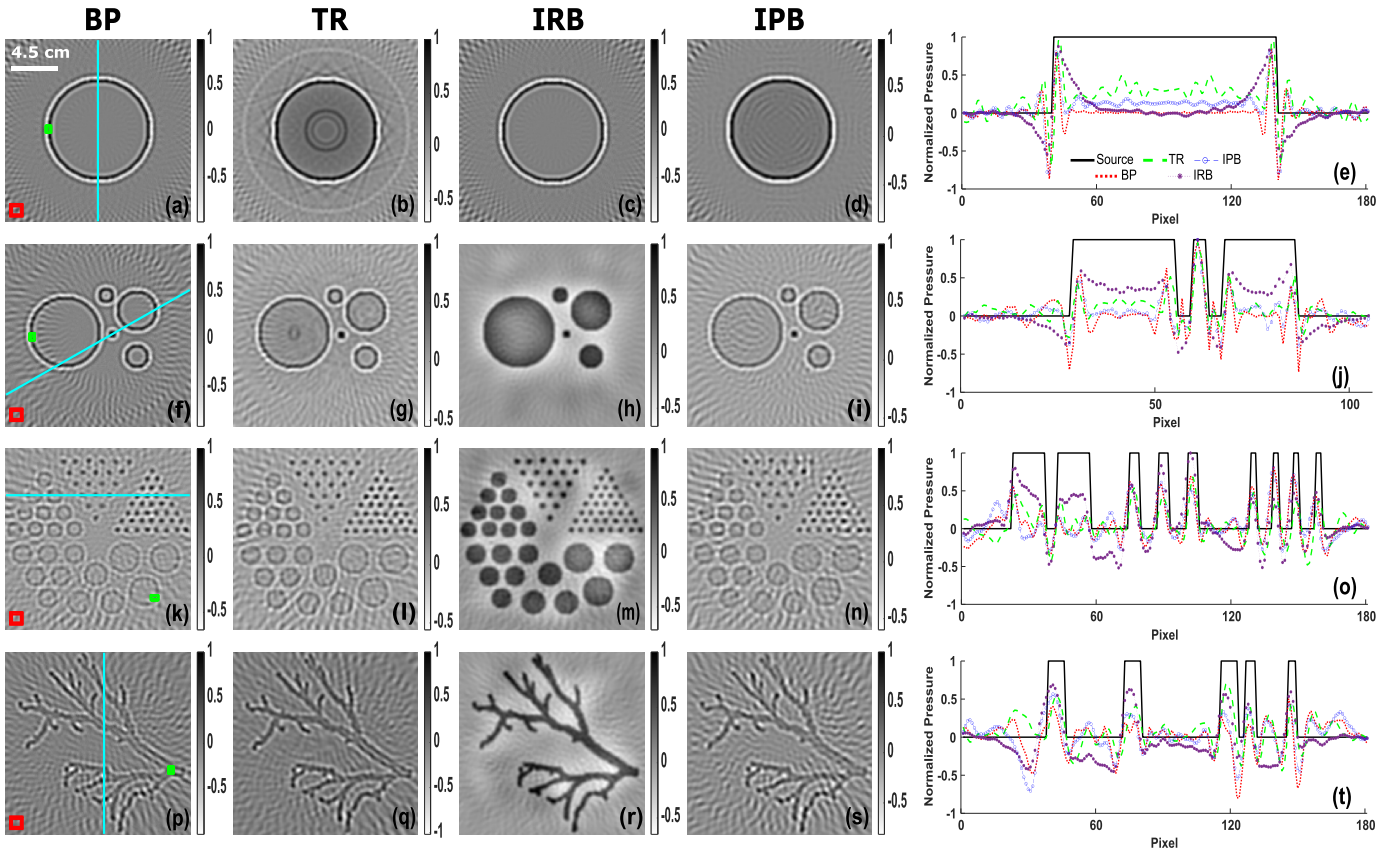


Fig. 5. Simulated images of the numerical phantoms considered in this study (k-Wave toolbox utilized to compute the PA signals). (a), (f), (k), and (p) BP method. (b), (g), (l), and (q) TR method. (c), (h), (m), and (r) IRB method. (d), (i), (n), and (s) IPB methods. (e), (j), (o), and (t) Line plots (pixel values along the cyan lines in the BP images). The roi and background regions are marked by green and red boxes, respectively.

TABLE II
QUANTITATIVE ASSESSMENT OF PERFORMANCE OF THE
RECONSTRUCTION TECHNIQUES FOR PA SIGNALS
COMPUTED BY THE K-WAVE TOOLBOX

Phantom	Metric	BP	TR	IRB	IPB
Disc	ERN	90.50	65.95	75.68	78.73
	PCC	0.13	0.66	0.60	0.44
	CNR	0.71	1.04	4.03	1.31
	SNR (dB)	11.90	20.87	27.56	10.27
Multiple discs	ERN	78.35	64.61	58.08	71.00
	PCC	0.17	0.53	0.73	0.37
	CNR	0.95	1.10	3.74	1.20
	SNR (dB)	15.74	16.72	28.90	11.24
Derenzo	ERN	89.58	81.16	71.05	86.60
	PCC	0.31	0.53	0.73	0.39
	CNR	0.69	0.60	3.44	0.93
	SNR (dB)	13.57	10.72	20.19	8.41
Vasculature	ERN	66.85	56.58	48.73	63.75
	PCC	0.30	0.55	0.72	0.40
	CNR	-0.03	0.85	17.54	0.58
	SNR (dB)	12.87	14.44	27.03	7.75

To validate the results presented here based on the PA signals generated by the discrete particle approach, we also conducted simulations using the k-Wave toolbox. The normalized reconstructed images are shown in Fig. 5 for different phantoms considered in this study. The reconstructed images are generally agree well with those of Fig. 4, and analogous

observations can be made. The image profile along the given lines also appears visually similar to those of the previous figure (see fifth columns of Figs. 4 and 5). However, the initial pressure for large objects and the k-Wave method decreases as we move from edge to the center, whereas it remains almost constant for the former approach [compare purple lines in Figs. 4(e) and 5(e)]. This difference diminishes as the object size decreases. This small discrepancy arises due to the fact that bandpass filters may be different in the two methods. The numerical values of the parameters for evaluating the performance of the image formation methods via k-Wave scheme are shown in Table II. The numerical values are, in general, agree well with those of Table I and thus standardises the discrete particle approach.

V. DISCUSSION AND CONCLUSION

In this work, phantoms have been created by placing acoustically homogeneous (compared to the ambient medium) monodisperse/polydisperse disks regularly or randomly within the imaging region. The PA signal emitted by a disk when illuminated by a delta function laser pulse can be calculated analytically. Therefore, PA signals from the individual disks at a detector location can be computed, and such signals may be added using the linear superposition principle to generate the resultant signal. These resultant signals computed at various

detector positions have been used for image reconstruction. This approach allows the handling of each cell individually. Therefore, contributions from different cells, with size dispersity and acoustic impedance heterogeneity, can be incorporated within the resultant signal. Note that the single particle approach took ≈ 6 min (105 s for the creation of vasculature phantom and 250 s for signal calculation for 100 detector locations) to execute. We found that time complexity for tissue simulation in this approach increased nonlinearly with the number of cells. For example, computation time increased about 1.8 and 4.2 times with the rise of number of particles from 18571 to 37142 and 297138 to 594275, respectively. The space complexity did not vary significantly over the entire range of number of particles tested (18571–594275). The single particle approach in conjunction with the Monte Carlo method can be realized in practice for PA signal simulation for tissue while keeping microscopic details intact.

The computation time of the k-Wave method was nearly 13 min though it modeled the PA source as a bulk medium. As discussed earlier, if tissue simulation is accomplished by placing individual cells within the blood vessel, subsequent PA signal computation would encounter enormously high time and space complexity in the k-Wave. The time complexity indeed increases nonlinearly with size of the computational domain. For instance, execution time increased from approximately 5 to 10 s when grid size was varied from 64×64 to 128×128 . However, the same quantity changed from nearly 8 to 74 min when grid size was varied from 1024×1024 to 2048×2048 . The space requirement remained almost constant even when the grid size was varied over a large span from 64×64 to 2048×2048 . The time and space complexity will further increase for 3D systems, and hence, the inclusion of microscopic details of tissue is not feasible in k-Wave simulation.

A Monte Carlo technique known as the sequential adsorption technique has been applied in this work to simulate a realization of a tissue sample. In this technique, location of a cell, if it is generated by a valid throw (i.e., satisfies nonoverlapping condition), becomes fixed. Therefore, it does not allow minor adjustment of positions of cells. As a result of that, tissue simulation may become difficult using this method particularly for dense medium (e.g., at 50% hematocrit). Another technique known as the Metropolis algorithm may be implemented for generating the random locations of RBCs [35], [36]. In this method, the positions of RBCs are updated continuously so that the tissue realization attains minimum energy state. This approach may be adapted to simulate dense tissue.

The individual PA source in this work has been assumed to be a uniform disk. This assumption is not always true. For example, the shape of normal RBC is biconcave, and the impact of shape may become visible at very high frequencies (hundreds of MHz). Closed-form expression for the PA signal for such a shape does not exist. Furthermore, the PA signal would become angle dependent (orientation dependent). Orientation-dependent PA signals from a normal RBC can be evaluated using Green's function approach when acoustic impedance mismatch is small. Nevertheless, tissue simulation considering the biconcave shape of RBCs would be nontrivial.

The BP algorithm is simple and fast but delivers the qualitative information of the imaging region only as pointed out earlier. The same is also true for the TR technique to some extent. The IRB algorithm seems to be the best algorithm among all. It can capture various properties of the imaging region (speed of sound) and detectors (geometry, size, frequency response, and sensitivity of profile of the aperture) while building the system matrix and thus provides faithful reconstruction. However, it may not produce good images for acoustically inhomogeneous imaging region. The sensors in the IPB algorithm are essentially treated as point detectors and, hence, may fail to generate accurate reconstruction for finite-size detectors. Moreover, in this method, pressure at a point depends on its strengths at the neighboring grid crossings. Therefore, grid crossings outside the source with $p_0 = 0$ also contribute to the estimation of p_0 inside the source, leading to the reduction of actual pressure within the source (see fourth columns of Figs. 4 and 5).

It may be noted that the standard form of (12) (i.e., L being the identity matrix) has been extensively used for PAT image reconstruction. However, a spatial normalized Laplacian filter has been considered herein while performing the Tikhonov regularization. We observed that slightly better image reconstruction, in general, can be achieved utilizing this approach. Furthermore, in this work, we have restricted ourselves to the bilinear interpolation only. However, other polynomial-based interpolation schemes also exist in the literature (namely, nearest neighbor, bicubic, biquintic, and so on) [37]. These methods have been extensively used by the image processing community. A separate investigation is required to study the performance of these interpolation techniques in PAT image reconstruction.

In conclusion, numerical phantoms were generated by inserting monodisperse/polydisperse disks of constant strength occupying regular or random locations within the imaging region. The PA signal from a single disk was calculated analytically, and then, such signals from many disks were summed up linearly to generate the resultant signal at a detector location. This step was repeated for all detector positions. The simulated signals were utilized to perform image reconstruction. Classical BP and TR techniques were implemented for image formation. Furthermore, model-based methods referred to as the IRB and IPB algorithms were also employed. Some standard parameters were computed to quantify the performance of each protocol. The discrete particle method facilitates the rapid computation of PA signals while retaining structural details of tissue in the microscopic level, and the IRB method emerges out to be the best reconstruction algorithm.

ACKNOWLEDGMENT

The computational results reported in this work were performed on the Central Computing Facility of IITA, Allahabad. The authors would also like to thank the members of the BMIL for constant support and help during the work. They also thank the anonymous reviewers for their comments that immensely helped them to improve the presentation as well as technical content of the work.

REFERENCES

- [1] L. V. Wang, *Photoacoustic Imaging and Spectroscopy*, vol. 4. Boca Raton, FL, USA: CRC Press, 2009, pp. 37–46.
- [2] P. K. Upputuri and M. Pramanik, “Recent advances toward preclinical and clinical translation of photoacoustic tomography: A review,” *J. Biomed. Opt.*, vol. 22, no. 4, Nov. 2016, Art. no. 041006.
- [3] L. V. Wang and J. Yao, “A practical guide to photoacoustic tomography in the life sciences,” *Nature Methods*, vol. 13, no. 8, pp. 627–638, Aug. 2016.
- [4] J. Tang, J. E. Coleman, X. Dai, and H. Jiang, “Wearable 3-D photoacoustic tomography for functional brain imaging in behaving rats,” *Sci. Rep.*, vol. 6, no. 1, Jul. 2016, Art. no. 25470.
- [5] P. K. Upputuri and M. Pramanik, “Dynamic *in vivo* imaging of small animal brain using pulsed laser diode-based photoacoustic tomography system,” *J. Biomed. Opt.*, vol. 22, no. 9, Sep. 2017, Art. no. 090501.
- [6] K. Jansen, G. van Soest, and A. F. W. van der Steen, “Intravascular photoacoustic imaging: A new tool for vulnerable plaque identification,” *Ultrasound Med. Biol.*, vol. 40, no. 6, pp. 1037–1048, Jun. 2014.
- [7] E. Fakhrejahani *et al.*, “Clinical report on the first prototype of a photoacoustic tomography system with dual illumination for breast cancer imaging,” *PLoS ONE*, vol. 10, no. 10, Oct. 2015, Art. no. e0139113.
- [8] I. Yamaga *et al.*, “Vascular branching point counts using photoacoustic imaging in the superficial layer of the breast: A potential biomarker for breast cancer,” *Photoacoustics*, vol. 11, pp. 6–13, Sep. 2018.
- [9] K. Sivasubramanian, V. Periyasamy, and M. Pramanik, “Non-invasive sentinel lymph node mapping and needle guidance using clinical hand-held photoacoustic imaging system in small animal,” *J. Biophotonics*, vol. 11, no. 1, Jan. 2018, Art. no. e201700061.
- [10] H. Kim and J. H. Chang, “Multimodal photoacoustic imaging as a tool for sentinel lymph node identification and biopsy guidance,” *Biomed. Eng. Lett.*, vol. 8, no. 2, pp. 183–191, May 2018.
- [11] V. Ntziachristos, “Going deeper than microscopy: The optical imaging frontier in biology,” *Nature Methods*, vol. 7, no. 8, pp. 603–614, Aug. 2010.
- [12] J. Weber, P. C. Beard, and S. E. Bohndiek, “Contrast agents for molecular photoacoustic imaging,” *Nature Methods*, vol. 13, no. 8, pp. 639–650, Aug. 2016.
- [13] Y. Liu, L. Nie, and X. Chen, “Photoacoustic molecular imaging: From multiscale biomedical applications towards early-stage theranostics,” *Trends Biotechnol.*, vol. 34, no. 5, pp. 420–433, May 2016.
- [14] M. Xu and L. V. Wang, “Universal back-projection algorithm for photoacoustic computed tomography,” *Phys. Rev. E, Stat. Phys. Plasmas Fluids Relat. Interdiscip. Top.*, vol. 71, no. 1, Jan. 2005, Art. no. 016706.
- [15] B. E. Treeby and B. T. Cox, “K-wave: MATLAB toolbox for the simulation and reconstruction of photoacoustic wave fields,” *J. Biomed. Opt.*, vol. 15, no. 2, 2010, Art. no. 021314.
- [16] C. B. Shaw, J. Prakash, M. Pramanik, and P. K. Yalavarthy, “Least squares QR-based decomposition provides an efficient way of computing optimal regularization parameter in photoacoustic tomography,” *J. Biomed. Opt.*, vol. 18, no. 8, Jul. 2013, Art. no. 080501.
- [17] M. Bhatt, S. Gutta, and P. K. Yalavarthy, “Exponential filtering of singular values improves photoacoustic image reconstruction,” *J. Opt. Soc. Amer. A, Opt. Image Sci.*, vol. 33, no. 9, pp. 1785–1792, 2016.
- [18] S. Gutta, S. K. Kalva, M. Pramanik, and P. K. Yalavarthy, “Accelerated image reconstruction using extrapolated tikhonov filtering for photoacoustic tomography,” *Med. Phys.*, vol. 45, no. 8, pp. 3749–3767, Aug. 2018.
- [19] A. Rosenthal, D. Razansky, and V. Ntziachristos, “Fast semi-analytical model-based acoustic inversion for quantitative photoacoustic tomography,” *IEEE Trans. Med. Imag.*, vol. 29, no. 6, pp. 1275–1285, Jun. 2010.
- [20] X. L. Dean-Ben, V. Ntziachristos, and D. Razansky, “Acceleration of photoacoustic model-based reconstruction using angular image discretization,” *IEEE Trans. Med. Imag.*, vol. 31, no. 5, pp. 1154–1162, May 2012.
- [21] X. L. Dean-Ben, A. Buehler, V. Ntziachristos, and D. Razansky, “Accurate model-based reconstruction algorithm for three-dimensional photoacoustic tomography,” *IEEE Trans. Med. Imag.*, vol. 31, no. 10, pp. 1922–1928, Oct. 2012.
- [22] N. A. Rejesh, H. Pullagurli, and M. Pramanik, “Deconvolution-based deblurring of reconstructed images in photoacoustic/thermoacoustic tomography,” *J. Opt. Soc. Amer. A, Opt. Image Sci.*, vol. 30, no. 10, pp. 1994–2001, Oct. 2013.
- [23] P. Warbal, M. Pramanik, and R. K. Saha, “Impact of sensor apodization on the tangential resolution in photoacoustic tomography,” *J. Opt. Soc. Amer. A, Opt. Image Sci.*, vol. 36, no. 2, pp. 245–252, 2019.
- [24] R. K. Saha and M. C. Kolios, “A simulation study on photoacoustic signals from red blood cells,” *J. Acoust. Soc. Amer.*, vol. 129, no. 5, pp. 2935–2943, May 2011.
- [25] G. J. Diebold, T. Sun, and M. I. Khan, “Photoacoustic monopole radiation in one, two and three dimensions,” *Phys. Rev. Lett.*, vol. 67, no. 24, pp. 3384–3387, 1991.
- [26] R. K. Saha and M. C. Kolios, “Effects of erythrocyte oxygenation on photoacoustic signals,” *J. Biomed. Opt.*, vol. 16, no. 11, 2011, Art. no. 115003.
- [27] R. K. Saha, S. Karmakar, and M. Roy, “Computational investigation on the photoacoustics of malaria infected red blood cells,” *PLoS ONE*, vol. 7, no. 12, Dec. 2012, Art. no. e51774.
- [28] R. K. Saha, “Computational modeling of photoacoustic signals from mixtures of melanoma and red blood cells,” *J. Acoust. Soc. Amer.*, vol. 136, no. 4, pp. 2039–2049, Oct. 2014.
- [29] S. Karmakar, M. Roy, and R. Saha, “Photoacoustic imaging of nanoparticle-containing cells using single-element focused transducer: A simulation study,” *IEEE Trans. Ultrason., Ferroelectr., Freq. Control*, vol. 62, no. 3, pp. 463–474, Mar. 2015.
- [30] R. K. Saha, “A simulation study on the quantitative assessment of tissue microstructure with photoacoustics,” *IEEE Trans. Ultrason., Ferroelectr., Freq. Control*, vol. 62, no. 5, pp. 881–895, Apr. 2015.
- [31] E. L. Hinrichsen, J. Feder, and T. Jøssang, “Random packing of disks in two dimensions,” *Phys. Rev. A, Gen. Phys.*, vol. 41, no. 8, pp. 4199–4209, Apr. 1990.
- [32] J. G. Berryman, “Random close packing of hard spheres and disks,” *Phys. Rev. A, Gen. Phys.*, vol. 27, no. 2, pp. 1053–1061, Feb. 1983.
- [33] M. Xu and L. V. Wang, “Analytic explanation of spatial resolution related to bandwidth and detector aperture size in thermoacoustic or photoacoustic reconstruction,” *Phys. Rev. E, Stat. Phys. Plasmas Fluids Relat. Interdiscip. Top.*, vol. 67, no. 5, May 2003, Art. no. 056605.
- [34] P. C. Hansen, “Regularization tools version 4.0 for MATLAB 7.3,” *Numer. Algorithms*, vol. 46, no. 2, pp. 189–194, Nov. 2007.
- [35] N. Metropolis, A. W. Rosenbluth, M. N. Rosenbluth, A. H. Teller, and E. Teller, “Equation of state calculations by fast computing machines,” *J. Chem. Phys.*, vol. 21, no. 6, pp. 1087–1092, Jun. 1953.
- [36] R. K. Saha and G. Cloutier, “Monte Carlo study on ultrasound backscattering by three-dimensional distributions of red blood cells,” *Phys. Rev. E, Stat. Phys. Plasmas Fluids Relat. Interdiscip. Top.*, vol. 78, no. 6, Dec. 2008, Art. no. 061919.
- [37] T. M. Lehmann, C. Gönner and Klaus Spitzer, “Survey: Interpolation methods in medical image processing,” *IEEE Trans. Med. Imag.*, vol. 18, no. 11, pp. 1049–1075, Nov. 1999.



Ravi Prakash was born in Gorakhpur, Uttar Pradesh, India. He received the Integrated Master of Technology (M.Tech.) degree in biomedical engineering from the Indian Institute of Information Technology Allahabad, Allahabad, India, in 2018.

In 2020, he joined IIT Hyderabad, Telangana, India, as a Research Scholar. His research interests include photoacoustic imaging and signal processing.



Divakar Badal received the Integrated M.Tech. degree in biomedical engineering from the Indian Institute of Information Technology Allahabad, Allahabad, India, in 2017. He is currently pursuing the Ph.D. degree with Centre for Biosystems Science and Engineering, Indian Institute of Science, Bengaluru, India.

His research interest includes understanding of microbial response to various physical stimuli in immunocompromised patients.



Avijit Paul received the Bachelor of Technology degree in computer science and engineering from the Kalyani Government Engineering College, West Bengal, India, in 2008, and the Masters in Intelligence Systems (CSE) degree from the University of Sussex, Brighton, U.K., in 2012.

He has more than 11 years of experience as a Software Developer, Technical Lead, and Project Lead in Tata Consultancy Services Ltd., Mumbai, India. He is currently with Biomedical

Imaging Laboratory, Department of Applied Sciences, Indian Institute of Information Technology Allahabad, Allahabad, India. His current research interests include biomedical imaging and signal processing in photoacoustics.



Deepak Sonker was born in Raebareli, Uttar Pradesh, India, in 1993. He received the Integrated Master of Technology degree in biomedical engineering from the Indian Institute of Information Technology Allahabad, Allahabad, India, in 2018. He is currently a graduate student at the University of Oulu, Oulu, Finland.

His research interests include biomedical optics and medical physics.



Ratan K. Saha (Member, IEEE) received the B.Sc. degree in physics from the University of North Bengal, Siliguri, India, in 1996, and the M.Sc. degree in physics from Jadavpur University, Kolkata, India, in 1999. He carried out his Ph.D. work at the Saha Institute of Nuclear Physics, Kolkata, from 2000 to 2006.

He was a Postdoctoral Fellow at the Laboratory of Biorheology and Medical Ultrasonics, Research Center of the University of Montreal Hospital, Montreal, QC, Canada, from 2007 to

2008; at the Department of Physics, Ryerson University, Toronto, ON, Canada, from 2009 to 2011; and at the Saha Institute of Nuclear Physics from 2011 to 2013. He was a CSIR Pool Officer at the Saha Institute of Nuclear Physics from 2013 to 2015. In 2015, he joined the Gurudas College, University of Calcutta, Kolkata, as an Assistant Professor. Since 2016, he has been an Assistant Professor with the Indian Institute of Information Technology Allahabad, Allahabad, India. His research interests include soft-tissue imaging and characterization with ultrasonics and photoacoustics.